

# Study of obtaining thin films of CeO<sub>2</sub> doped with 2 and 4 mol% of europium, terbium and thulium by spin coating: photocatalytic properties

*(Estudo da obtenção de filmes finos de CeO<sub>2</sub> dopados com 2 e 4 %mol de európio, térbio e túlio por spin coating: propriedades fotocatalíticas)*

B. P. Dias<sup>1</sup>, N. F. Andrade Neto<sup>1\*</sup>, L. M. P. Garcia<sup>1</sup>, M. R. D. Bomio<sup>1</sup>, F. V. Motta<sup>1</sup>

<sup>1</sup>Federal University of Rio Grande do Norte, Department of Materials Engineering,

Laboratory of Chemical Synthesis of Materials, P.O. Box 1524, Natal, RN, Brazil

## Abstract

In this study, thin films of Eu<sup>3+</sup>, Tb<sup>3+</sup> and Tm<sup>3+</sup> doped CeO<sub>2</sub> in the proportions of 2 and 4 mol% were obtained by spin coating and calcined at 700 °C. The films were characterized by XRD, SEM, AFM and UV-vis techniques. The photocatalytic activity of the thin films was measured by the degradation of the methylene blue (MB) dye. The thin films were submitted to 4 photocatalytic cycles to analyze the capacity to be reused. XRD patterns showed no secondary phase formation, where all characteristic peaks were related to CeO<sub>2</sub>. SEM micrographs indicated that doping at 4 mol% promoted the reduction in the thickness and surface porosity of the thin films. AFM images indicated the increase in surface roughness with rare earths doping. Doping with Eu<sup>3+</sup>, Tb<sup>3+</sup> and Tm<sup>3+</sup> increased the degradation of the methylene blue dye by at least 15% for thin films doped at 4 mol%. The reuse tests indicated that the photocatalytic activity remained practically constant even with the application of four consecutive cycles.

**Keywords:** Eu<sup>3+</sup>, Tb<sup>3+</sup> and Tm<sup>3+</sup> doped CeO<sub>2</sub>, thin films, spin coating, photocatalytic reuse.

## Resumo

Neste estudo, filmes finos de CeO<sub>2</sub> dopados com Eu<sup>3+</sup>, Tb<sup>3+</sup> e Tm<sup>3+</sup> nas proporções de 2 e 4 %mol foram obtidos por spin coating e calcinados em 700 °C. Os filmes foram caracterizados pelas técnicas de DRX, MEV, MFA e UV-vis. As propriedades fotocatalíticas dos filmes finos foram determinadas pela degradação do corante azul de metileno (AM). Os filmes finos foram submetidos a 4 ciclos fotocatalíticos para analisar a capacidade de serem reusados. Os difratogramas de raios X mostraram que não houve a formação de fases secundárias, onde todos os picos foram referentes ao CeO<sub>2</sub>. As micrografias de MEV indicaram que a dopagem com 4 %mol promoveu a redução da espessura e porosidade superficial dos filmes finos. As imagens de MFA indicaram o aumento da rugosidade superficial com a dopagem utilizando terras raras. A dopagem com Eu<sup>3+</sup>, Tb<sup>3+</sup> e Tm<sup>3+</sup> aumentaram a atividade fotocatalítica em pelo menos 15% para os filmes dopados com 4 %mol. Os testes de reuso indicaram que a atividade fotocatalítica se manteve praticamente constante após a aplicação de quatro ciclos consecutivos.

**Palavras-chave:** CeO<sub>2</sub> dopado com Eu<sup>3+</sup>, Tb<sup>3+</sup> e Tm<sup>3+</sup>, filmes finos, spin coating, reuso fotocatalítico.


## INTRODUCTION

The growing increase in waste generation from the industries causes the need for constant studies on fast and efficient treatment methods. Waste from textile industries receives special attention because they contain a high amount of organic dyes, which are difficult to treat [1]. Dyes discarded in the wild without proper treatment may alter the local fauna and flora, preventing the marine environment from receiving an adequate amount of light [1, 2]. The use of heterogeneous photocatalysis for the treatment of these dyes is considered the most efficient method, as it converts these organic compounds into H<sub>2</sub>O, CO<sub>2</sub> and mineral salts

[3]. Heterogeneous photocatalysis is usually used with a semiconductor material acting as a catalyst, where it acts to produce reactive oxygen species (ROS), such as hydroxyl radicals (<sup>•</sup>OH) and superoxides (<sup>•</sup>O<sub>2</sub>), which have a high oxidative capacity against organic contaminants [4, 5].

Recent studies indicate CeO<sub>2</sub> as an effective photocatalyst [6]. Among its main characteristics are the high chemical resistance and the photocorrosion, high capacity of absorption of UV radiation and an excellent capacity of liberation and storage of oxygen [7]. Moreover, the ease of conversion between cerium valences (Ce<sup>4+</sup>/Ce<sup>3+</sup>) makes it a material with high redox potential [8, 9]. However, in comparison to other materials used in photocatalysis, such as TiO<sub>2</sub>, it presents low mobility of charges on its surface, which makes the photocatalytic process difficult [9]. Modifications in the electronic structure of CeO<sub>2</sub>,

\*netoandrade@ufrn.edu.br

 <https://orcid.org/0000-0003-1421-2904>

such as doping, generate defects that alter the mobility of the charges, increasing its photocatalytic activity [10]. The introduction of rare earth ions into the  $\text{CeO}_2$  lattice potentiates their intrinsic properties due to the replacement of  $\text{Ce}^{4+}$  by trivalent cations, which increase the amount of oxygen vacancies and introduce intermediate levels between the valence and conduction bands [11, 12]. The increase in the oxygen vacancy number provides the impediment in the  $e^-/h^+$  pair recombination generated in the photocatalytic process, increasing its effect [13].

Nanoparticulate materials have higher photocatalytic activity than the others due to the greater available surface area [14]. However, due to the small scale, they become a problem for the separation after the catalytic process [15]. The use of supported materials, such as thin films, eliminates this problem. In this work, the photocatalytic activity of  $\text{CeO}_2$  thin films against methylene blue (MB) dye was optimized by doping with rare earth ions ( $\text{Eu}^{3+}$ ,  $\text{Tb}^{3+}$  and  $\text{Tm}^{3+}$ ) in the 2 and 4 mol% proportions. To analyze the ability of the films to be reused after a photocatalytic cycle, they were submitted to four consecutive cycles, without any treatment on its surface.

## MATERIALS AND METHODS

Cerium nitrate [ $\text{Ce}(\text{NO}_3)_3$ , Sigma Aldrich], europium nitrate [ $\text{Eu}(\text{NO}_3)_3$ , Alfa Aesar], terbium nitrate [ $\text{Tb}(\text{NO}_3)_3$ , Alfa Aesar], thulium nitrate [ $\text{Tm}(\text{NO}_3)_3$ , Alfa Aesar], ethylene glycol ( $\text{C}_2\text{H}_6\text{O}_2$ , Alfa Aesar), citric acid ( $\text{C}_6\text{H}_8\text{O}_7$ , Synth), isopropyl alcohol ( $\text{C}_3\text{H}_8\text{O}$ , Alfa Aesar), ammonium hydroxide ( $\text{NH}_4\text{OH}$ , Synth) and deionized water were used to obtain the precursor solutions. For the preparation of the cerium precursor solution, citric acid was dissolved in deionized water at 70 °C; after complete dissolution, cerium nitrate was added. Finally, ethylene glycol was added and the temperature was maintained at 70 °C until the solution achieved a viscosity of 25 cps. Obtaining the europium, terbium and thulium doped cerium solutions occurred similarly, where the cerium cations were stoichiometrically substituted at 2 and 4 mol% ( $\text{Ce}_{(1-x)}\text{A}_{(x)}\text{O}_2$  with  $\text{A} = \text{Ce}, \text{Tb}, \text{Tm}$ ).

The silicon (100) substrates were washed with deionized water and isopropyl alcohol in an ultrasonic bath. Subsequently, the substrates were immersed in a solution of deionized water, ammonium hydroxide and hydrogen peroxide ( $\text{H}_2\text{O}_2$ , Synth), heated to 70 °C. The precursor solutions were deposited on the silicon substrates by spin coating technique, without heating. The rotation speed and spin time were fixed at 700 rpm for 3 s and 7200 rpm for 30 s, using a commercial spinner (Chemat Techn., KW-4B spin-coater). After deposition of each layer, the samples were taken to calcination at 700 °C (heating rate of 5 °C/min), where they remained for 1 h, and were cooled inside the furnace. In all samples, three layers of thin films were deposited, according to the scheme shown in Fig. 1.

In order to identify the present phases, the X-ray diffraction (XRD) technique was used, operating at a low angle, with a speed of 1 °/min and a 0.01° step in a Shimadzu

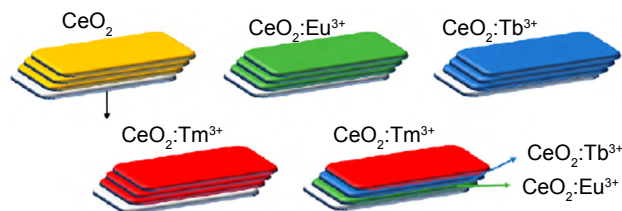


Figure 1: Schemes of thin films obtained by spin coating.

[Figura 1: Esquemas dos filmes finos obtidos por spin coating.]

diffractometer (XRD-6000) using  $\text{CuK}\alpha$  radiation (1.5418 Å). For more information on the crystallinity of the thin films, the crystallite size was estimated using Scherrer's equation [16]. The morphological aspects of the films were observed by field emission scanning electron microscopy (SEM). The film thickness was determined with the use of ImageJ software [17]. The chemical composition of the films was analyzed by energy-dispersive X-ray spectroscopy (EDX). Atomic force microscopy (AFM) was performed to obtain more information about the surface roughness of thin films. UV-vis spectroscopy was performed on a Shimadzu spectrophotometer (UV-2550) operating in the diffuse reflectance mode, with wavelength ranging from 200 to 900 nm. Kubelka-Munk function [18] was used to convert the reflectance data into absorbance and the Wood and Tauc method [19] was used for the estimation of band gap ( $E_{\text{gap}}$ ). For these films, the direct transition was admitted.

The photocatalytic activity of the thin films was estimated by varying the concentration of the methylene blue dye by the test time. For this, the samples were illuminated by six UVC lamps (Phillips, 15 W, with maximum intensity at 254 nm=4.9 eV). Thin films with dimensions of 6x6 mm (receiving irradiance of 2.5 MW/m<sup>2</sup>) were submerged in a quartz beaker (15 mm diameter) containing 10 mL of the methylene blue dye (MB,  $\text{C}_{16}\text{H}_{18}\text{ClN}_3\text{S}$ , Mallinckrodt, with purity of 99.5%) without stirring, with a concentration of  $10^{-5} \text{ mol}\cdot\text{L}^{-1}$  and pH 5, and 0.06 mL of  $\text{H}_2\text{O}_2$ . The temperature was monitored throughout the process and remained at about 27 °C. At 1 min intervals, an aliquot was withdrawn for analysis of the variation of the dye concentration. To eliminate the adsorption effects, the thin films remained for 24 h in contact with MB dye without contact with light sources. The reuse tests were performed by placing the thin films in contact with another MB solution with  $10^{-5} \text{ mol}\cdot\text{L}^{-1}$  concentration. The photocatalytic tests were performed in duplicates and the mean values were used.

## RESULTS AND DISCUSSION

Fig. 2 shows the XRD patterns obtained for  $\text{CeO}_2$  thin films, pure and doped with  $\text{Eu}^{3+}$ ,  $\text{Tb}^{3+}$  and  $\text{Tm}^{3+}$ , in the proportions of 2% (Fig. 2a) and 4% (Fig. 2b) obtained by spin coating. All peaks were related to cubic  $\text{CeO}_2$  and spatial group Fm-3m, characterized by ICSD 72155 file. No secondary peaks were observed, indicating that  $\text{Eu}^{3+}$ ,  $\text{Tb}^{3+}$  and  $\text{Tm}^{3+}$  ions were well incorporated into the  $\text{CeO}_2$  lattice. According to Fig. 2, the displacements of the peaks were

observed with doping, indicating the introduction of  $\text{Eu}^{3+}$ ,  $\text{Tb}^{3+}$  and  $\text{Tm}^{3+}$  ions into  $\text{CeO}_2$  lattice. Doping with materials of different valences and ionic radius tend to cause changes in the crystalline lattice that may go unnoticed when analyzed only visually, especially when doping occurs in low concentrations [20].

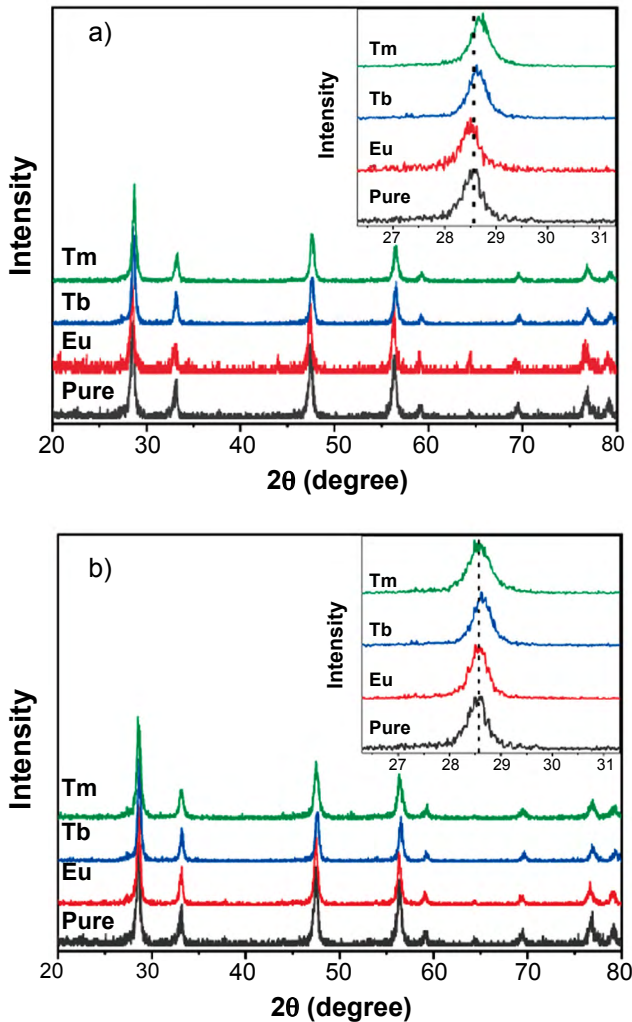


Figure 2: XRD patterns for  $\text{CeO}_2$  thin films, pure and doped with 2% (a) and 4% (b) of  $\text{Eu}^{3+}$ ,  $\text{Tb}^{3+}$  and  $\text{Tm}^{3+}$ .

[Figura 2: Difratoogramas de raios X dos filmes finos de  $\text{CeO}_2$  puro e dopados com 2% (a) e 4% (b) de  $\text{Eu}^{3+}$ ,  $\text{Tb}^{3+}$  e  $\text{Tm}^{3+}$ .]

Table I presents the crystallite sizes obtained by the Scherrer equation; according to the values obtained, the doping with  $\text{Eu}^{3+}$  and  $\text{Tb}^{3+}$  promoted an increase in the size of the crystallite, whereas the doping with  $\text{Tm}^{3+}$  provided a small reduction. Rodrigues et al. [21] showed that the doping of  $\text{CeO}_2$  with  $\text{Eu}^{3+}$  provides an increase in crystallite size due to the difference between the ionic radius of  $\text{Ce}^{4+}$  ions by  $\text{Eu}^{3+}$ , which have an ionic radius of 0.87 and 0.95 Å, respectively. Sahoo et al. [22] also showed that the replacement of  $\text{Ce}^{4+}$  ions by  $\text{Eu}^{3+}$  generates oxygen vacancy in the crystalline structure of  $\text{CeO}_2$  reducing the crystallite size. The addition of  $\text{Tb}^{3+}$ , which has an ionic radius of 0.92 Å, increases the crystallite due to the generation of oxygen vacancies [23]. The reduction

in the crystallite size of  $\text{CeO}_2$  when doped with  $\text{Tm}^{3+}$  occurs because this ion has the same size of ionic radius and act on the surface of the crystal, hindering its growth [24].

Table I - Crystallite size and microdeformation obtained by the Scherrer's equation.

[Tabela I - Tamanho de cristalito e microdeformação obtidos pela equação de Scherrer.]

Sample	Crystallite size (nm)	Microdeformation, $\epsilon \times 10^{-4}$
Pure $\text{CeO}_2$	17.54	4.20
$\text{CeO}_2$ :2%Eu	20.84	3.92
$\text{CeO}_2$ :2%Tb	22.41	3.62
$\text{CeO}_2$ :2%Tm	17.22	4.23
$\text{CeO}_2$ :4%Eu	20.84	3.91
$\text{CeO}_2$ :4%Tb	23.16	3.51
$\text{CeO}_2$ :4%Tm	17.37	4.22

Figs. 3 and 4 show the top view and transverse section of  $\text{CeO}_2$  thin films doped with  $\text{Eu}^{3+}$ ,  $\text{Tb}^{3+}$  and  $\text{Tm}^{3+}$  and the  $\text{CeO}_2$  and  $\text{CeO}_2$ :Eu:Tb:Tm thin films, respectively. The EDX analysis and the chemical mapping performed on the  $\text{CeO}_2$ :4%Eu:Tb:Tm thin film are shown in Figs. 4d and 4e. The thickness of the films was measured along its entire length. The mean value of film thickness, as well as the standard deviation, is shown in Table II. It was noticed that the films were dense and homogeneous, presenting low values of standard deviation for thickness. Doping of

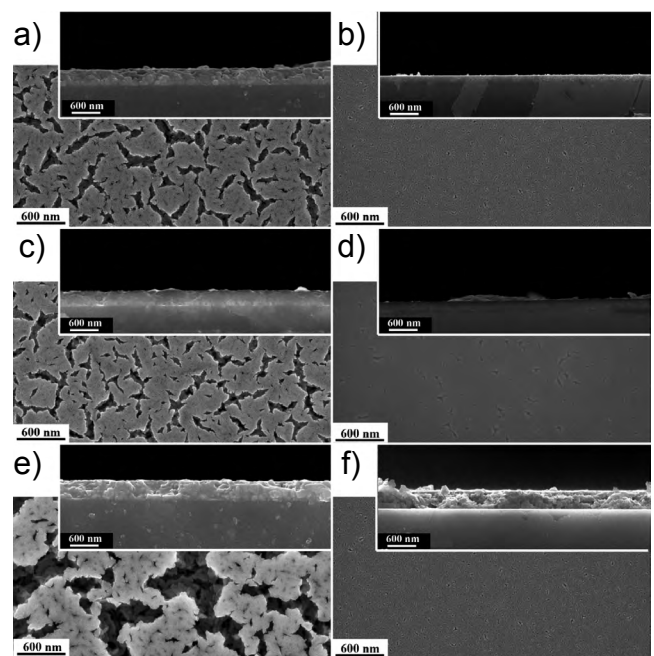


Figure 3: Top view and transverse section SEM images of the thin films of  $\text{CeO}_2$ :2%Eu (a),  $\text{CeO}_2$ :4%Eu (b),  $\text{CeO}_2$ :2%Tb (c),  $\text{CeO}_2$ :4%Tb (d),  $\text{CeO}_2$ :2%Tm (e), and  $\text{CeO}_2$ :4%Tm (f).

[Figura 3: Imagens de MEV de vista de topo e seção transversal dos filmes finos de  $\text{CeO}_2$ :2%Eu (a),  $\text{CeO}_2$ :4%Eu (b),  $\text{CeO}_2$ :2%Tb (c),  $\text{CeO}_2$ :4%Tb (d),  $\text{CeO}_2$ :2%Tm (e) e  $\text{CeO}_2$ :4%Tm (f).]

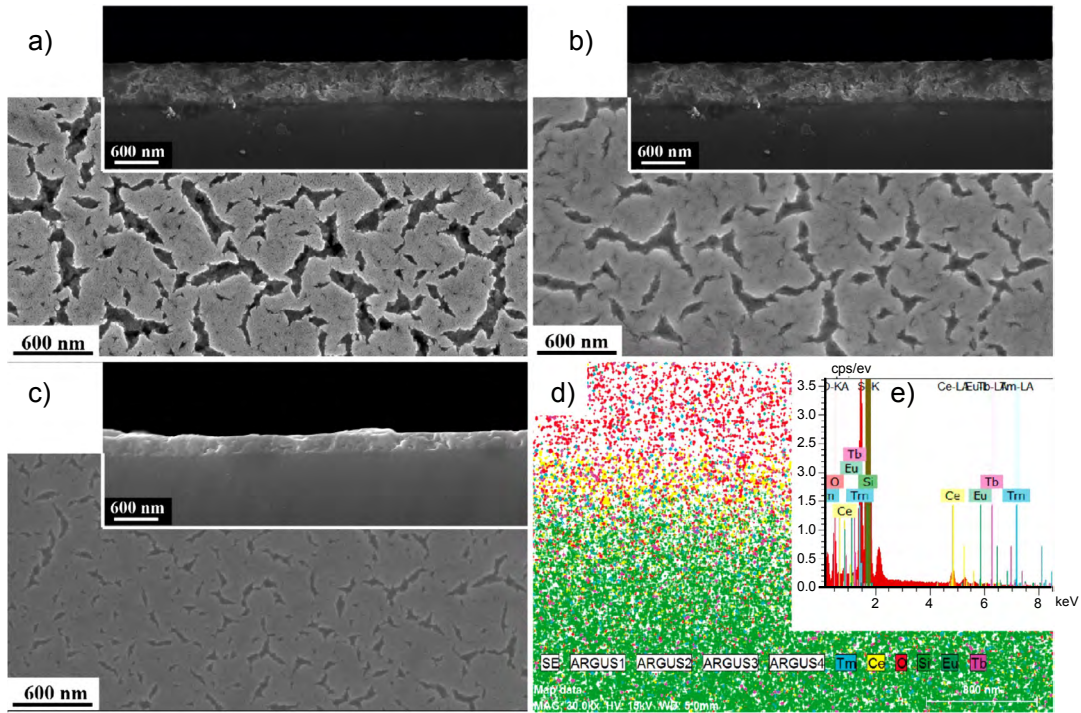


Figure 4: Top view and transverse section SEM images of the thin films of  $\text{CeO}_2$  (a),  $\text{CeO}_2:2\%\text{Eu:Tb:Tm}$  (b),  $\text{CeO}_2:4\%\text{Eu:Tb:Tm}$  (c), and elemental mapping (d) and EDX spectrum (e) of  $\text{CeO}_2:4\%\text{Eu:Tb:Tm}$  thin film.

[Figura 4: Imagens de MEV de vista de topo e seção transversal dos filmes finos de  $\text{CeO}_2$  (a),  $\text{CeO}_2:2\%\text{Eu:Tb:Tm}$  (b),  $\text{CeO}_2:4\%\text{Eu:Tb:Tm}$  (c), e mapeamento elemental (d) e espectro de EDX (e) para o filme fino  $\text{CeO}_2:4\%\text{Eu:Tb:Tm}$ .]

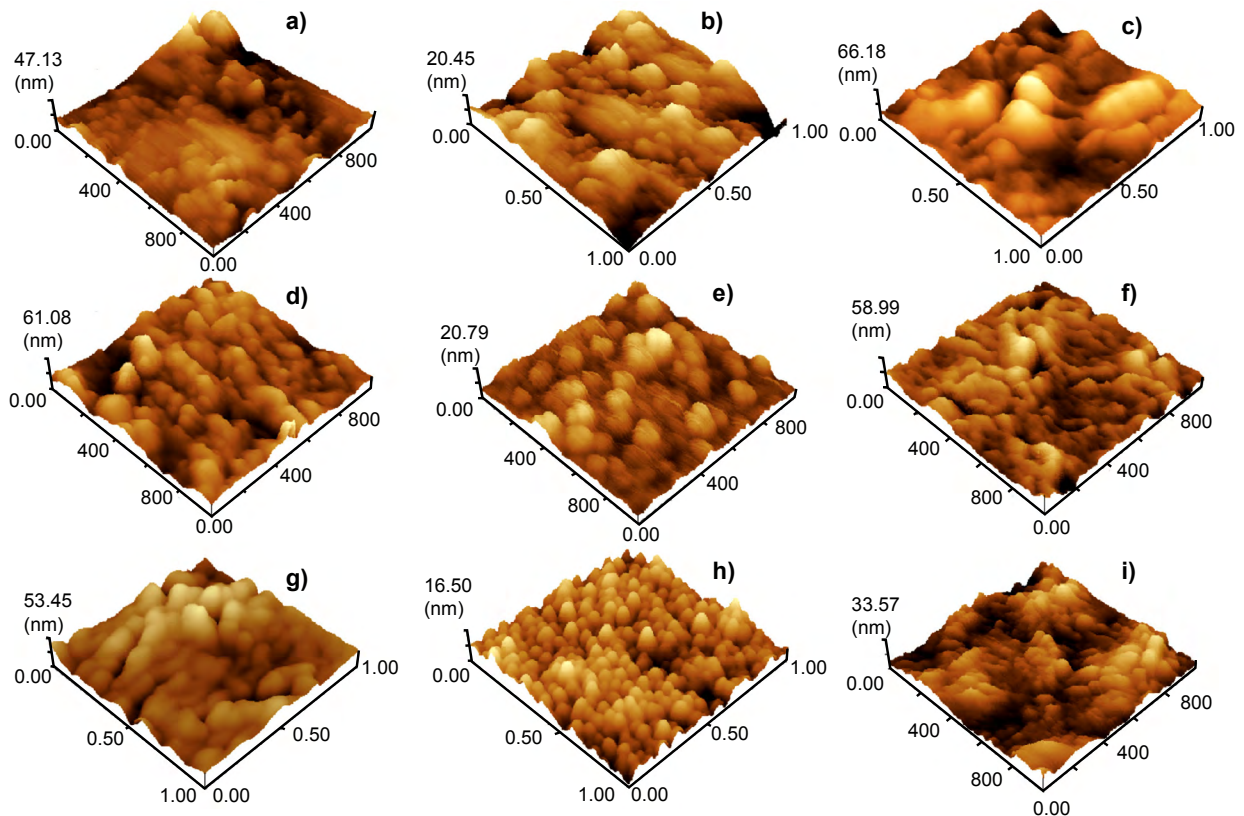


Figure 5: AFM images for the thin films of  $\text{CeO}_2$  (a),  $\text{CeO}_2:2\%\text{Eu}$  (b),  $\text{CeO}_2:4\%\text{Eu}$  (c),  $\text{CeO}_2:2\%\text{Tb}$  (d),  $\text{CeO}_2:4\%\text{Tb}$  (e),  $\text{CeO}_2:2\%\text{Tm}$  (f),  $\text{CeO}_2:4\%\text{Tm}$  (g),  $\text{CeO}_2:2\%\text{Eu:Tb:Tm}$  (h), and  $\text{CeO}_2:4\%\text{Eu:Tb:Tm}$  (i).

[Figura 5: Imagens de MFA para os filmes finos de  $\text{CeO}_2$  (a),  $\text{CeO}_2:2\%\text{Eu}$  (b),  $\text{CeO}_2:4\%\text{Eu}$  (c),  $\text{CeO}_2:2\%\text{Tb}$  (d),  $\text{CeO}_2:4\%\text{Tb}$  (e),  $\text{CeO}_2:2\%\text{Tm}$  (f),  $\text{CeO}_2:4\%\text{Tm}$  (g),  $\text{CeO}_2:2\%\text{Eu:Tb:Tm}$  (h) e  $\text{CeO}_2:4\%\text{Eu:Tb:Tm}$  (i).]

Table II - Average thickness of the CeO<sub>2</sub> thin films obtained by spin coating.

[Tabela II - Espessura média dos filmes finos de CeO<sub>2</sub> obtidos por spin coating.]

Sample	Average thickness of thin film (nm)
Pure CeO <sub>2</sub>	556±8
CeO <sub>2</sub> :2%Eu	307±6
CeO <sub>2</sub> :2%Tb	325±2
CeO <sub>2</sub> :2%Tm	409±11
CeO <sub>2</sub> :2%Eu:Tb:Tm	346±9
CeO <sub>2</sub> :4%Eu	139±2
CeO <sub>2</sub> :4%Tb	142±6
CeO <sub>2</sub> :4%Tm	388±19
CeO <sub>2</sub> :4%Eu:Tb:Tm	262±7

thin films of CeO<sub>2</sub> with rare earths promoted a reduction in its thickness; this reduction was more evident in the films doped with europium. According to [25], the reduction in the thickness of CeO<sub>2</sub> thin film occurred due to the difference between the ionic radius of the Ce<sup>4+</sup> and the rare earths. The increase in the rare earth concentration from 2% to 4% promoted higher densification of the films. Higher densification, coupled with reduced thin film thickness, provided less void space, making films ideal for sensitive applications such as gas sensors and photocatalysis [26]. The increase in the densification of thin films doped with 4% of rare earth occurred due to the interaction with the cerium ions, causing coalescence and grain growth to occur with the course of the calcination [27]. The EDX mapping for the CeO<sub>2</sub>:4%Eu:Tb:Tm sample indicated that rare earth ions were properly incorporated.

Fig. 5 shows the 3D micrographs obtained by AFM for pure CeO<sub>2</sub> and doped with the rare earths. It was observed that doping increased the surface roughness and promoted

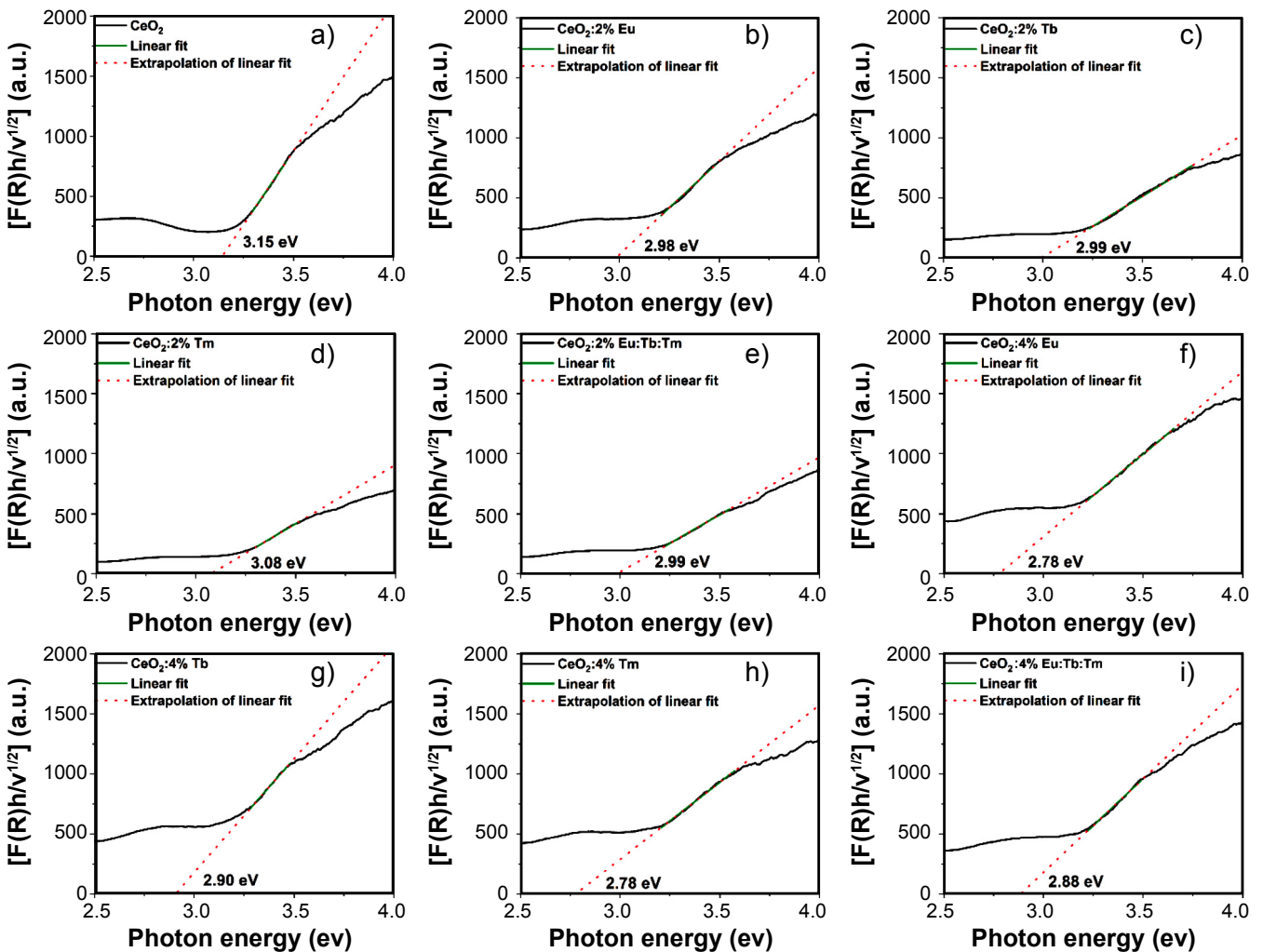


Figure 6: UV-vis absorbance spectra for the thin films of CeO<sub>2</sub> (a), CeO<sub>2</sub>:2%Eu (b), CeO<sub>2</sub>:2%Tb (c), CeO<sub>2</sub>:2%Tm (d), CeO<sub>2</sub>:2%Eu:Tb:Tm (e), CeO<sub>2</sub>:4%Eu (f), CeO<sub>2</sub>:4%Tb (g), CeO<sub>2</sub>:4%Tm (h), and CeO<sub>2</sub>:4%Eu:Tb:Tm (i).

[Figura 6: Espectros de absorvância UV-vis para os filmes finos de CeO<sub>2</sub> (a), CeO<sub>2</sub>:2%Eu (b), CeO<sub>2</sub>:2%Tb (c), CeO<sub>2</sub>:2%Tm (d), CeO<sub>2</sub>:2%Eu:Tb:Tm (e), CeO<sub>2</sub>:4%Eu (f), CeO<sub>2</sub>:4%Tb (g), CeO<sub>2</sub>:4%Tm (h) e CeO<sub>2</sub>:4%Eu:Tb:Tm (i).]

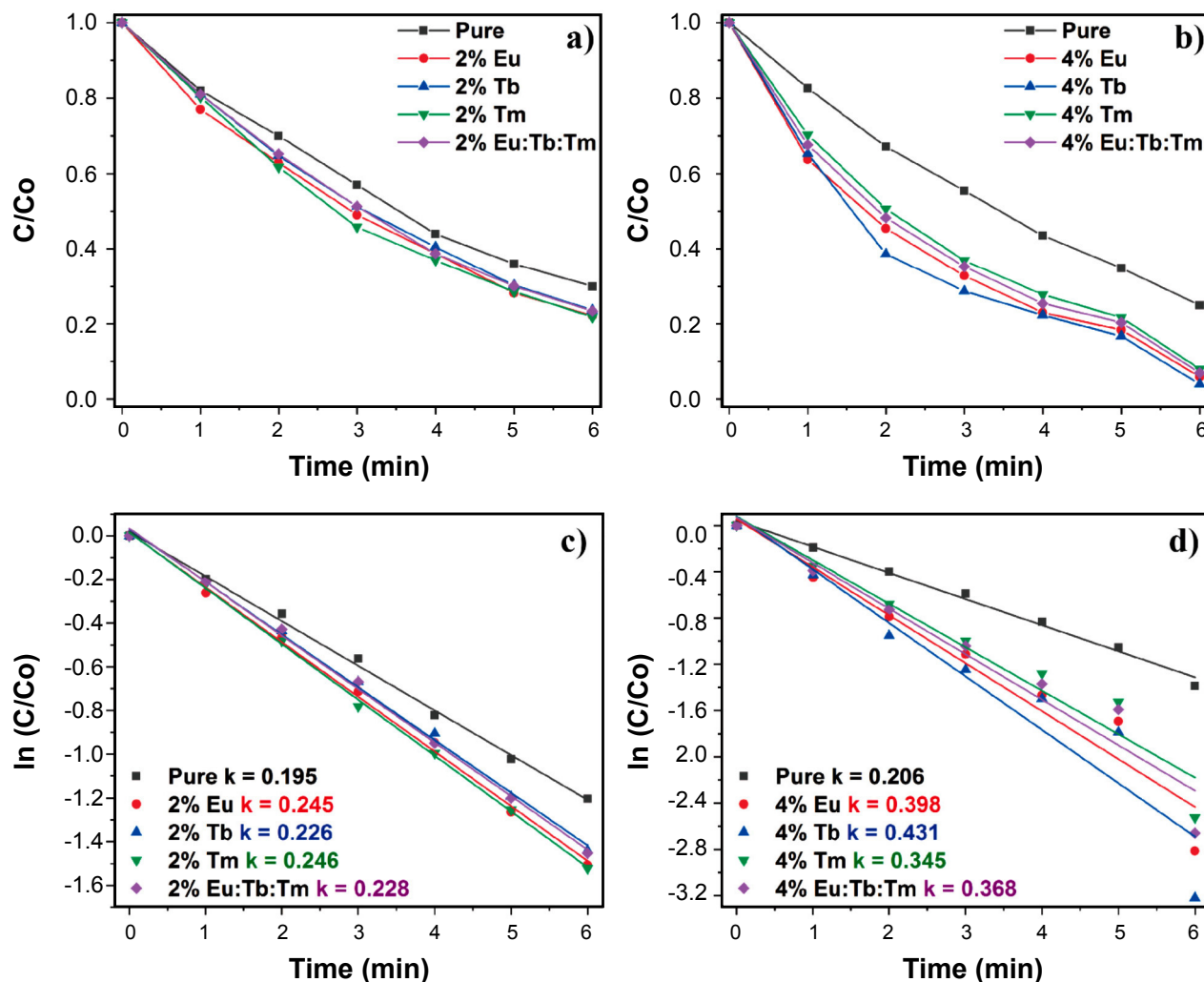


Figure 7: Variation of the MB dye concentration with time for the samples doped with 2% (a) and 4% (b) of  $\text{Eu}^{3+}$ ,  $\text{Tb}^{3+}$  and  $\text{Tm}^{3+}$ , and respective first-order kinetic plots (c,d).

[Figura 7: Variação da concentração do corante AM com o tempo para as amostras dopadas com 2% (a) e 4% (b) de  $\text{Eu}^{3+}$ ,  $\text{Tb}^{3+}$  e  $\text{Tm}^{3+}$  e respectivos gráficos de cinética de primeira ordem (c,d).]

the appearance of more  $\text{CeO}_2$  sites on the surface of the films, indicating that rare earth ions assisted nucleation and grain growth [28]. Rare earth ions are chemically active and easily adsorbed onto the substrate surface, then attracting the  $\text{CeO}_2$  molecules by van der Waals forces for rapid nucleation [29]. The thin films composed by  $\text{Eu:Tb:Tm}$  formed more bonds with  $\text{CeO}_2$ , obtaining smaller grains and, consequently, greater roughness [30].

Fig. 6 shows the absorbance extrapolation curves by photon energy for  $E_{\text{gap}}$  estimation. According to the values shown in Fig. 6, it is observed that the  $E_{\text{gap}}$  of the thin films obtained in this study ranged between 2.78 and 3.15 eV. These values were in accordance with the  $E_{\text{gap}}$  reported in the literature for  $\text{CeO}_2$  [31, 32]. From Fig. 6, it can be seen that the increase in dopant concentration led to the reduction in  $E_{\text{gap}}$  of the  $\text{CeO}_2$  films.  $E_{\text{gap}}$  of semiconductor materials is directly related to the presence of defects in the crystalline lattice. The oxygen vacancies act to form intermediate levels below the states of the band 4f, where this occupation

depends on the temperature and defects concentration [32]. Wang et al. [33] studied the effect of the calcination temperature in the presence of oxygen vacancies in the  $\text{CeO}_2$  lattice and showed that increasing this temperature from 550 to 850 °C increases the concentration of oxygen vacancies. The defects introduced into the  $\text{CeO}_2$  lattice by the rare earths together with the temperature of 700 °C used in the calcination of thin films in this study can be attributed as those responsible for the presence of oxygen vacancies.

Fig. 7 shows the curves of the variation of MB dye concentration by time, assembled from the absorbance curves. From Figs. 7a and 7b, it can be seen that doping with the rare earths provided the increase in the photocatalytic activity of the thin films. The photocatalytic activity of semiconductor materials is directly related to the generation of reactive oxygen species (ROS), which have a high oxidative capacity [4]. The generation of ROS occurs when the material receives enough energy to excite the electron of the valence band for the conduction band, forming electron/

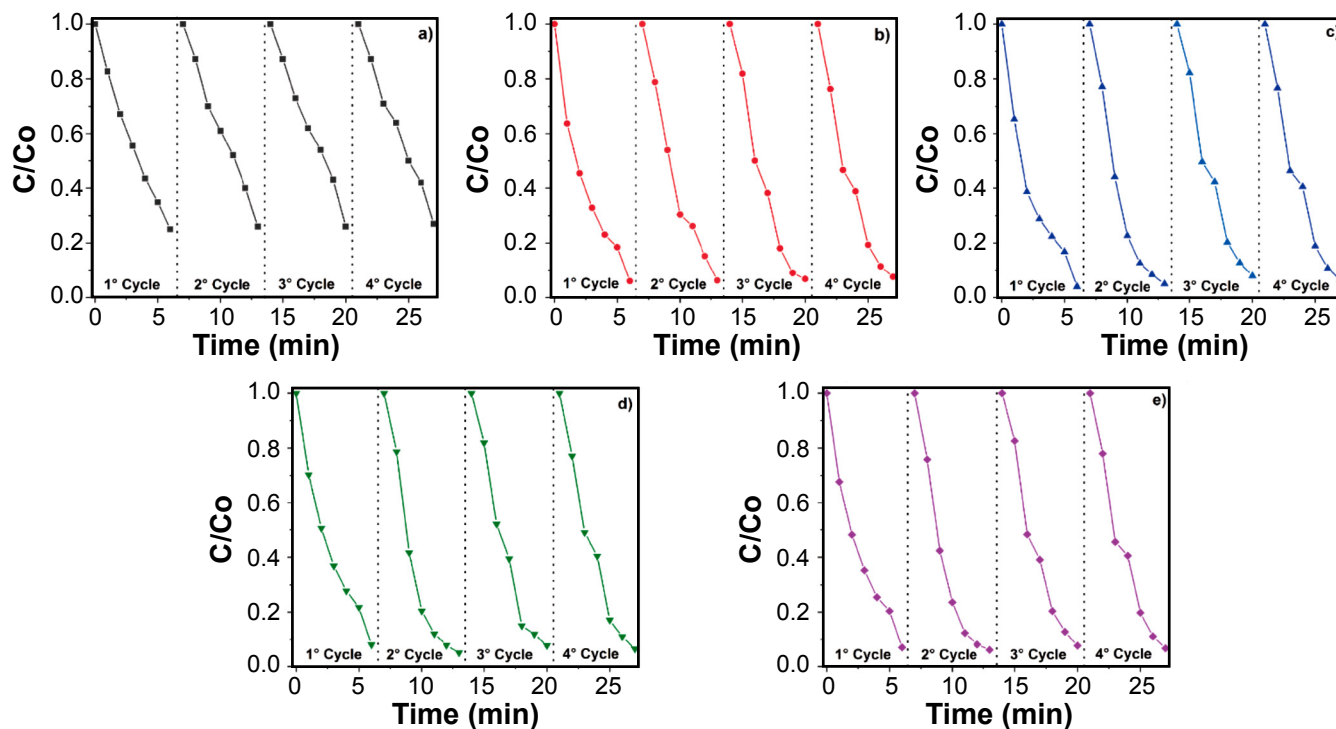


Figure 8: Photocatalytic reuse for the thin films of  $\text{CeO}_2$  (a),  $\text{CeO}_2:4\%\text{Eu}$  (b),  $\text{CeO}_2:4\%\text{Tb}$  (c),  $\text{CeO}_2:4\%\text{Tm}$  (d), and  $\text{CeO}_2:4\%\text{Eu:Tb:Tm}$  (e).  
 [Figura 8: Reuso fotocatalítico para os filmes finos de  $\text{CeO}_2$  (a),  $\text{CeO}_2:4\%\text{Eu}$  (b),  $\text{CeO}_2:4\%\text{Tb}$  (c),  $\text{CeO}_2:4\%\text{Tm}$  (d), and  $\text{CeO}_2:4\%\text{Eu:Tb:Tm}$  (e).]

hole pairs ( $e^-/h^+$ ) [34, 35]. The photocatalytic process may be described by a first-order kinetic model with relation to the absorbance of methylene blue [36], and the results obtained are shown in Figs. 7c and 7d. The graphs show the linear relationship of  $\ln(C/C_0)$  by the irradiation time. From this linear relationship, Eq. A was used and the kinetic constant determined:

$$-\ln \frac{C_t}{C_0} = k \cdot t \quad (\text{A})$$

where  $C_t$  is the absorbance of methylene blue at time  $t$ ,  $C_0$  the initial absorbance,  $t$  the irradiation time, and  $k$  the kinetic constant. As discussed previously, the doping with  $\text{Eu}^{3+}$ ,  $\text{Tb}^{3+}$  e  $\text{Tm}^{3+}$  provided the formation of oxygen vacancies due to the differences in valence and ionic radius with  $\text{Ce}^{4+}$  [22-25]. Oxygen vacancies act in a way to restrict the recombination of the  $e^-/h^+$  pairs, increasing the amount of ROS available and, consequently, the photocatalytic activity of the thin films [37]. The doping of  $\text{CeO}_2$  with rare earths proved to be very efficient, where the 4% terbium sample reduced the MB dye concentration by 96%, while the pure  $\text{CeO}_2$  sample reduced by 75%. Correia et al. [38] obtained  $\text{TiO}_2$  and  $\text{Bi}_2\text{O}_3$  thin films which reduced approximately 10% of the initial MB dye concentration after 310 min. The kinetic constants,  $k$ , allowed the observation of the first wave behavior of the curves, where it was evident the increase of this by doping with the rare earths.

The use of thin films for the treatment of effluents is important because it avoids the generation of secondary residues after the photocatalytic process, since the catalyst

is fixed in the substrate. Thus, it is important to analyze the ability of these materials to be reused in consecutive processes without the need for treatment. According to [39], the evaluation of the reusability of the catalyst consists of two criteria: i) maintenance of the photocatalytic activity with the course of the cycles; and ii) ease of the catalyst being recycled from the solution. As the catalyst is immobilized on the substrate, the evaluation of the reusability of the ceria thin films is related to the capacity to maintain the photocatalytic activity with the course of the cycles. Fig. 8 shows the curves of the variation of the concentration of the MB dye by the time, during four cycles of the test without any treatment between them. As can be seen, all the films maintained their photocatalytic activity during the course of four test cycles, indicating their viability for photocatalytic applications in several cycles.

## CONCLUSIONS

Spin coating technique, allied with the temperature of 700 °C used in the calcination, was efficient to obtain thin films of pure  $\text{CeO}_2$  and doped with rare earths (Eu, Tb and Tm), without the formation of secondary phases. The increase in doping from 2 to 4 mol% produced thinner films, with lower surface porosity and greater roughness. The defects generated by the doping reduced the band gap ( $E_{\text{gap}}$ ) of  $\text{CeO}_2$  thin films. The increase of the defects increased the ionic conduction of the films, favoring the photocatalytic activity, which increased about 5% for films doped with 2 mol% and 15% for films doped with 4 mol% of rare earths. The reuse tests showed that the films maintained their photocatalytic

activity after 4 consecutive cycles, without considerable losses, being indicated for long term applications.

## ACKNOWLEDGMENTS

This study was partially financed by the Coordenação de Aperfeiçoamento de Pessoal de Nível Superior - Brasil (CAPES/PROCAD) - Finance Code 2013/2998/2014. The authors also thank the financial support from the Brazilian research funding institution: CNPq No. 307546/2014.

## REFERENCES

- [1] F. Teran, *Rev. Monogr. Amb.* **13** (2014) 3316.
- [2] E. Duarte, T.P. Xavier, D.R. de Souza, J. de Miranda, A.H. Machado, C. Jung, L. de Oliveira, C. Sattler, *Quím. Nova* **28** (2005) 921.
- [3] H. Sopha, M. Baudys, M. Krbal, R. Zazpe, J. Prikryl, J. Krysa, J.M. Macak, *Electrochem. Commun.* **97** (2018) 91.
- [4] P. Arbab, B. Ayati, M.R. Ansari, *Process Saf. Environ.* **121** (2019) 87.
- [5] A. Bianco Prevot, V. Maurino, D. Fabbri, A.M. Braun, M.C. Gonzalez, *Catal. Today*, *in press*.
- [6] R. Magudieswaran, J. Ishii, K.C.N. Raja, C. Terashima, R. Venkatachalam, A. Fujishima, S. Pitchaimuthu, *Mater. Lett.* **239** (2019) 40.
- [7] D. van Dao, T.T.D. Nguyen, H.-Y. Song, J.-K. Yang, T.-W. Kim, Y.-T. Yu, I.-H. Lee, *Mater. Design* **159** (2018) 186.
- [8] M.M. Khan, S.A. Ansari, J.-H. Lee, M.O. Ansari, J. Lee, M.H. Cho, *J. Colloid Interface Sci.* **431** (2014) 255.
- [9] J.C. Cano-Franco, M. Álvarez-Láinez, *Mater. Sci. Semicon. Proc.* **90** (2019) 190.
- [10] Z. Wang, X. Li, H. Qian, S. Zuo, X. Yan, Q. Chen, C. Yao, *J. Photochem. Photobiol. A* **372** (2019) 42.
- [11] M.A. Rodrigues, A.C. Catto, E. Longo, E. Nossol, R.C. Lima, *J. Rare Earths* **36** (2018) 1074.
- [12] W. Huang, Y. Tan, D. Li, H. Du, X. Hu, G. Li, Y. Kuang, M. Li, D. Guo, *J. Lumin.* **206** (2019) 432.
- [13] K.M. Girish, R. Naik, S.C. Prashantha, H. Nagabhushana, H.P. Nagaswarupa, K.S. Anantha Raju, H.B. Premkumar, S.C. Sharma, B.M. Nagabhushana, *Spectrochim. Acta A* **138** (2015) 857.
- [14] Y. AlSalka, A. Hakki, M. Fleisch, D.W. Bahnemann, *J. Photochem. Photobiol. A* **366** (2018) 81.
- [15] K. Piccoli, M. Scaliante, N. Fernandes-Machado, in *Blucher Chem. Eng. Proc.* **1** (2015) 1553.
- [16] P. Kumar, P. Kumar, A. Kumar, R.C. Meena, R. Tomar, F. Chand, K. Asokan, *J. Alloys Compd.* **672** (2016) 543.
- [17] C.A. Schneider, W.S. Rasband, K.W. Eliceiri, *Nat. Methods* **9** (2012) 671.
- [18] L. Tolvaj, K. Mitsui, D. Varga, *Wood Sci. Technol.* **45** (2011) 135.
- [19] D.L. Wood, J. Tauc, *Phys. Rev. B* **5** (1972) 3144.
- [20] P. Kumar, B. Ahmad, F. Chand, K. Asokan, *Appl. Surf. Sci.* **452** (2018) 217.
- [21] M.A. Rodrigues, A.C. Catto, E. Longo, E. Nossol, R.C. Lima, *J. Rare Earths* **36** (2018) 1074.
- [22] S.K. Sahoo, M. Mohapatra, S. Anand, *J. Korean Phys. Soc.* **62** (2013) 297.
- [23] A.A. Saleh, H.Z. Hamamera, H.K. Khanfar, A.F. Qasrawi, G. Yumusak, *Mater. Sci. Semicon. Proc.* **88** (2018) 256.
- [24] L.G.A. Carvalho, L.A. Rocha, J.M.M. Buarque, R.R. Gonçalves, C.S. Nascimento Jr, M.A. Schiavon, S.J.L. Ribeiro, J.L. Ferrari, *J. Lumin.* **159** (2015) 223.
- [25] R. Aydin, B. Sahin, *Ceram. Int.* **44** (2018) 22249.
- [26] O. Kamoun, A. Boukhachem, M. Amlouk, S. Ammar, *J. Alloys Compd.* **687** (2016) 595.
- [27] G.M. Ramans, J.V. Gabrusenoks, A.R. Lasis, A.A. Patmalnieks, *J. Non-Cryst. Solids* **90** (1987) 637.
- [28] R. Rajesh Kanna, K. Sakthipandi, S.M. Seeni Mohamed Aliar, N. Lenin, M. Sivabharathy, *J. Rare Earths* **36** (2018) 1299.
- [29] W. Shi, Z. Li, L. Wang, S. Wu, G. Zhang, M. Meng, X. Ma, *Opt. Commun.* **406** (2018) 50.
- [30] M. Wang, B. Tian, D. Yue, W. Lu, M. Yu, C. Li, Q. Li, Z. Wang, *J. Rare Earths* **33** (2015) 355.
- [31] M. Mittal, A. Gupta, O.P. Pandey, *Sol. Energy* **165** (2018) 206.
- [32] B. Li, B. Zhang, S. Nie, L. Shao, L. Hu, *J. Catal.* **348** (2017) 256.
- [33] K. Wang, Y. Chang, L. Lv, Y. Long, *Appl. Surf. Sci.* **351** (2015) 164.
- [34] L. Chen, J. Tang, L.-N. Song, P. Chen, J. He, C.-T. Au, S.-F. Yin, *Appl. Catal. B* **242** (2019) 379.
- [35] C. Belver, J. Bedia, A. Gómez-Avilés, M. Peñas-Garzón, J.J. Rodriguez, in "Nanoscale mater. water purification", S. Thomas, D. Pasquini, S.-Y. Leu, D.A. Gopakumar (Eds.), Elsevier (2019) 581.
- [36] M.M. Momeni, M. Hakimian, A. Kazempour, *Ceram. Int.* **41** (2015) 13692.
- [37] F. Bensouici, M. Bououdina, A.A. Dakhel, R. Tala-Ighil, M. Tounane, A. Iratni, T. Souier, S. Liu, W. Cai, *Appl. Surf. Sci.* **395** (2017) 110.
- [38] F.C. Correia, M. Calheiros, J. Marques, J.M. Ribeiro, C.J. Tavares, *Ceram. Int.* **44** (2018) 22638.
- [39] L.M.P. Garcia, M.T.S. Tavares, N.F. Andrade Neto, R.M. Nascimento, C.A. Paskocimas, E. Longo, M.R.D. Bomio, F.V. Motta, *J. Mater. Sci.: Mater. Electron.* **29** (2018) 6530.
- (Rec. 04/01/2019, Rev. 08/03/2019, 27/03/2019, Ac. 02/04/2019)